OPTICS

Holographic metasurface gas sensors for instantaneous visual alarms

Inki Kim[1†], Won-Sik Kim[2†], Kwan Kim[3], Muhammad Afnan Ansari[4], Muhammad Qasim Mehmood[4], Trevon Badloe[1], Yeseul Kim[1], Junho Gwak[1], Heon Lee[3], Young-Ki Kim[2]*, Junsuk Rho[1,2,5]*

The rapid detection of biological and chemical substances in real time is particularly important for public health and environmental monitoring and in the military sector. If the process of substance detection to visual reporting can be implemented into a single miniaturized sensor, there could be a profound impact on practical applications. Here, we propose a compact sensor platform that integrates liquid crystals (LCs) and holographic metasurfaces to autonomously sense the existence of a volatile gas and provide an immediate visual holographic alarm. By combining the advantage of the rapid responses to gases realized by LCs with the compactness of holographic metasurfaces, we develop ultracompact gas sensors without additional complex instruments or machinery to report the visual information of gas detection. To prove the applicability of the compact sensors, we demonstrate a metasurface-integrated gas sensor on safety goggles via a one-step nanocasting process that is attachable to flat, curved, and flexible surfaces.

INTRODUCTION

The rapid detection of biological and chemical substances in real time is an emerging research field related to modern public health and environmental monitoring, with implications in the military sector. There are various methods of detecting target substances and corresponding sensor platforms such as reading out electrical (*1*), optical (*2*, *3*), and radio-frequency/microwave signal changes (*4*). Among the sensor platforms, liquid crystal (LC)–based sensors are particularly suitable candidates for sensitive, real time, and rapid detections (*5*, *6*). The innate characteristics of LCs, i.e., soft, tunability, optical amplification, and stimuli responsiveness, make them a preferable method of detecting gases, volatile organic compounds, and biomolecules (*7*–*11*), which can have negative and even fatal effects on the health of human beings. Most previous LC sensors have been designed to confirm the presence or absence of target molecules by checking the degree of transmittance using a polarizing optical microscope that is controlled by the LC ordering transition upon partitioning of the target molecules. However, such a complex measurement method is considered to be one of the major obstacles in the implementation of portable and compact sensor systems.

The arrangement of ultrathin metallic or dielectric nanostructures into arrays of artificial metaatoms, often called optical metasurfaces, has been used for ultracompact displays and photonic sensor platforms (*12*–*14*). Most early metasurface sensors are based on metallic nanostructures, or plasmonic metasurfaces (*15*–*18*), to exploit the strongly focused light to amplify distinct signals from a target molecule, such as fluorescence (*19*), Raman (*20*, *21*), and infrared (IR) absorption signals (*22*–*24*), or to clearly observe resonance wavelength shifts (*16*, *17*). More recently, to overcome the inherent limitations of plasmonic metasurfaces due to ohmic losses and low quality factors (Q factors), all dielectric metasurfaces with high Q factors have been actively studied (*25*–*27*). For instance, a pixelated dielectric metasurface platform, where multiple sharp resonance peaks from each metasurface pixel tightly cover the mid-IR regime, is introduced (*25*). For target molecules that show specific molecular absorption fingerprints (e.g., distinct IR absorption spectra), unique barcode-like images of intensity contrast can be confirmed through the pixelated metasurface platform. Furthermore, a platform that can detect target molecules with high sensitivity based on a pixelated metasurface has been reported, but it requires extra instrumentation and corresponding image processing technology (*26*). Switchable metasurfaces with phase change materials (e.g., VO_2, $Ge_2Sb_2Te_5$, Mg, and WO_3) that respond to specific stimuli (e.g., hydrogen and temperature) have also been introduced (*28*–*32*). Because a target stimulus is predetermined by the material characteristics, it limits diverse applications. For instance, the phase transition temperatures are relatively high [VO_2: >80°C (*30*), $Ge_2Sb_2Te_5$: >150°C (*31*)] demanding external power sources and the optical modulation is mainly in the near-IR regime. Moreover, the switching response times for the phase transitions of Mg (*28*, *29*) or WO_3 (*32*) are limited by the chemical reactions (i.e., the absorption or desorption of reactants).

Here, we propose a compact sensor platform that combines LCs with holographic metasurfaces, termed as LC-integrated metasurface (LC-MS), to promptly sense a volatile gas and provide instantaneous feedback through a visual holographic alarm as depicted in Fig. 1A. This technology integrates the advantages of the stimuli responsiveness of LCs and the compactness of metasurfaces while maximizing the effectiveness of the sensor by providing gas sensing information through the use of a visual holographic alarm without the need for any further complex instrumentation. The metasurface hologram (or metahologram) is made of hydrogenated amorphous silicon (a-Si:H) and is designed to reproduce different holographic images according to the polarization of incident light and maximizes the polarization conversion efficiency by simultaneously using the

[1]Department of Mechanical Engineering, Pohang University of Science and Technology (POSTECH), Pohang 37673, Republic of Korea. [2]Department of Chemical Engineering, Pohang University of Science and Technology (POSTECH), Pohang 37673, Republic of Korea. [3]Department of Materials Science and Engineering, Korea University, Seoul 02841, Republic of Korea. [4]Department of Electrical Engineering, Information Technology University of the Punjab, Lahore 54600, Pakistan. [5]National Institute of Nanomaterials Technology (NINT), Pohang 37673, Republic of Korea.
*Corresponding author. Email: jsrho@postech.ac.kr (J.R.); ykkim@postech.ac.kr (Y.-K.K.)
†These authors contributed equally to this work.

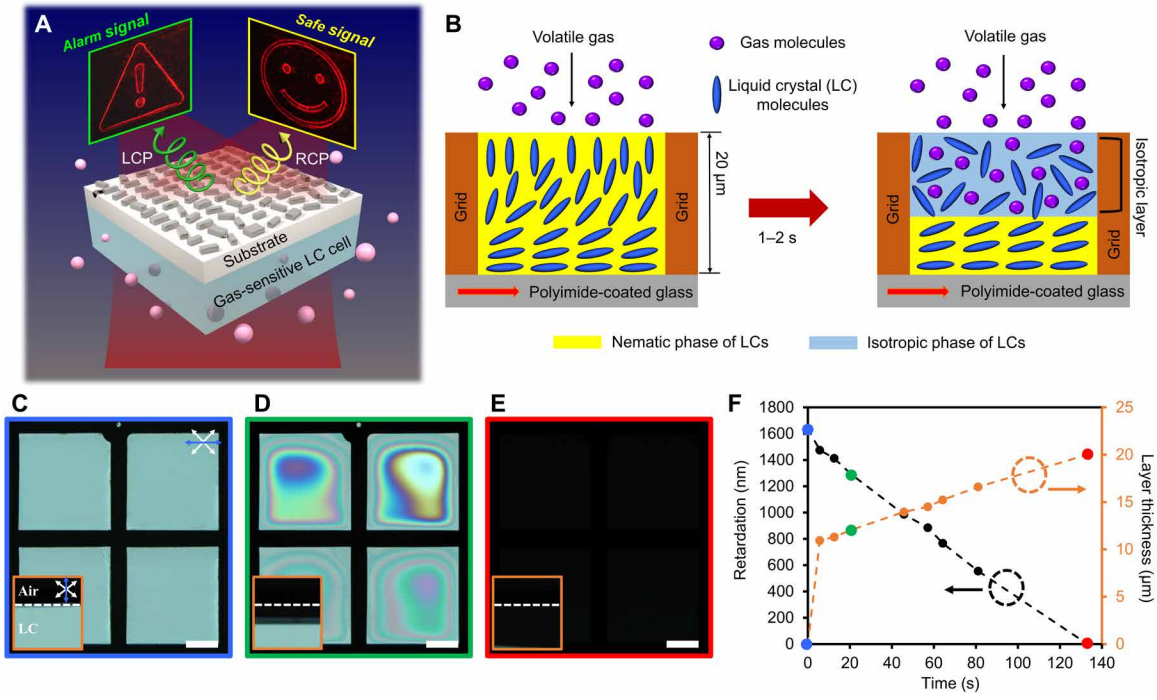

Fig. 1. Design of gas-responsive liquid crystal (LC) cells and their optical responses. (**A**) Schematic of the proposed holographic metasurface gas sensor platform. A holographic metasurface integrated with gas-responsive LCs projects a safety signal (smiley face) in the absence of a target dangerous gas, while an alarm signal (exclamation mark) is displayed upon the detection of the gas. Right circularly polarized (RCP; yellow arrow) illumination creates a "safe signal," and left circularly polarized (LCP; green arrow) illumination produces an "alarm signal." (**B**) Schematic illustration (side view) of gas-responsive LCs that are hosted in a microwell. Initially, the LC cell has a hybrid anchoring configuration because of the vertical orientation of the LCs at the air interface and the unidirectional tangential orientation set by the rubbed polyimide coated onto a glass substrate. When volatile gases are introduced, however, the LC ordering is lowered because the isotropic gas molecules partition into the LC layer. Consequently, the nematic-to-isotropic phase transition occurs from the air interface and the isotropic layer expands as more gas molecules are diffused into the LCs. (**C** to **E**) Sequential optical micrographs (top) of the LC cell upon the exposure of IPA gas; see movie S1. Scale bar, 100 μm. The insets in (C) to (E) show the corresponding side view micrographs. The LC cell is placed in a closed chamber with a concentration of IPA gas of around 200 ppm. White arrows represent the polarization of the polarizer (input) and analyzer (output). Blue arrows represent the rubbing direction. (**F**) Measured retardation and calculated isotropic layer thickness over time. Data corresponding to (C) to (E) are marked by the blue, green, and red dots.

geometric and propagation phase of each nanostructure. Such a strategy substantially improves the diffraction efficiency and effectively reduces any undesired afterimage, which consequently provides clearer visual information with high fidelity. Accordingly, the LC-MS is optimized to transmit different polarization states of light depending on the presence or absence of the volatile gases. Furthermore, to realize a pragmatic conformal sensor that can be attached to any surface regardless of it being flat or curved, the metasurface is implemented on a flexible substrate using a one-step nanocasting process to confirm the feasibility of such an attachable conformal sensor.

RESULTS AND DISCUSSION

Design of gas-responsive LC cells

The molecular ordering of LCs, an anisotropic medium with long-range molecular ordering, has been proven to be controllable through a variety of external stimuli. The preferred orientation of LCs is described by the director $\hat{\mathbf{n}}$, and the degree of orientation is expressed by the order parameter $S = \langle \frac{1}{2}(3\cos^2\theta - 1) \rangle$, where θ is the angle between $\hat{\mathbf{n}}$ and the molecular axis (*33*, *34*). S is temperature dependent and decreases as the temperature increases, inducing a more randomly ordered state. In a perfectly ordered crystal, $S = 1$ as the molecular axes are aligned parallel to $\hat{\mathbf{n}}$, while $S = 0$ for an isotropic liquid. Generally, in an LC phase, S is in the range of $0.2 \leq S \leq 0.8$, with the nematic phase in the range of $0.5 \leq S \leq 0.7$ (*35*). The phase retardation of light passing through the LC medium is modulated by the LC ordering. The reordering of LCs changes the effective refractive index (Δn_{eff}) in the LC cell as $\Delta n_{\text{eff}} = (n_o n_e / \sqrt{n_e^2 \cos^2\alpha + n_o^2 \sin^2\alpha}) - n_o$, where n_e and n_o are the extraordinary and ordinary refractive index of the LC, respectively, and α represents the angle between $\hat{\mathbf{n}}$ and the substrate normal ($\alpha = 0°$ indicates vertical orientation). In general, the phase retardation τ can be expressed as $\tau = \int_0^l 2\pi\Delta n_{\text{eff}}(z)/\lambda dz$, where l is the thickness of the LC cell and λ is the wavelength of light. Consequently, the desired output beam polarization state can be adjusted by τ of the LC cells (*33*–*37*).

To realize the volatile gas sensing LC systems that transform the polarization of transmitted light, we first observe and characterize the gas responsiveness of the LCs in the simplest geometry, where a microwell structure (thickness of about 20 μm) is filled with nematic LCs, i.e., 4-cyano-4′-pentylbiphenyl (5CB) as described in Fig. 1B. The bottom glass substrate was coated with a polyimide and then rubbed to obtain a unidirectional tangential orientation with a pretilted angle of 3.8°. As the air interface causes the LCs to be orientated vertically (*6*–*9*), the LC cell has the hybrid anchoring configuration (Fig. 1B) exhibiting a bright optical texture between crossed polarizers

with the rubbing direction of 45° from the optic axes of polarizers (Fig. 1C). The initial hybrid configuration is designed to transmit right circularly polarized (RCP) light for incident RCP light by setting $\tau \approx 2\pi N$, where N is integer. Using a Bereck compensator, the retardance of our cell is measured to be 1637.52 nm corresponding to 6π for $\lambda = 550$ nm at 25°C (a more detailed explanation can be found in Materials and Methods) (*33*, *36*).

As a target hazardous gas for detection, we use an isopropyl alcohol (IPA) gas because it is typically used as a cleaning solution in the industry (*38*). The toxicity of IPA is well known to cause stomach pain, confusion, dizziness, and slowed breathing. In the semiconductor industry, IPA is suspected to be one of the main causes of leukemia (*39*). The current permissible exposure limit (PEL) of IPA is 400 parts per million (ppm) by the Occupational Safety and Health Administration of the United States.

Upon the exposure of IPA gas at the constant concentration (C_{IPA}) of 200 ppm in a closed chamber, we observe the LC cell to exhibit the transition from white (Fig. 1C) to colored (Fig. 1, D to F) within a few seconds and end up with black optical appearances 140 s after the exposure of IPA gas (Fig. 1, E and F, and movie S1). It indicates that the IPA gas molecules had diffused into the LCs, thus lowering the LC ordering. Consequently, the nematic to isotropic phase transition occurs from the air interface and the resulting isotropic layer expands toward the glass interface, as shown in Fig. 1 (C to E). These results demonstrate the capability of the LC cell to promptly sense a toxic gas and convert the polarization of the transmitted light, as evidenced by the measure of τ to gradually decrease over exposure time (Fig. 1F). The thickness of the induced isotropic layer is also extracted from the measure of τ, which is in a good agreement with the optical transition (Fig. 1, C to E); the director of 5CB is tilted to about 26.5° at the nematic-isotropic interface (*40*–*42*). We make two additional observations to investigate the optical behavior of 5CB film with respect to the type and dosage of gas. First, the response rate of the LC cell is dependent on C_{IPA}. While the entire 5CB film becomes an isotropic phase at ~140 s for $C_{IPA} = 200$ ppm, the phase transition ends at shorter time periods for higher C_{IPA} of 400 ppm (within 40 s; movie S2). The C_{IPA}-dependent optical response in LCs is responsible for the fact that the diffusion of more gas molecules into the LCs lowers their molecular ordering faster. We note that the polarization conversion of transmitted light from RCP to left circularly polarization (LCP) (i.e., when $\Delta\tau = \lambda/2$ for $\lambda = 633$ nm) for the switching of holographic image occurs at ~18 s for $C_{IPA} \approx 200$ ppm (Fig. 1, C to F) and at ~7 s for $C_{IPA} \approx 400$ ppm (movie S2). Second, the optical response of LCs is also dependent on the type of gas exposed, as each gas molecule has different diffusion coefficients and intermolecular interactions with LCs. To demonstrate the response rates of LCs depending on the type and dosage of gas, we conduct experiments with seven different gases generated by evaporating solvents in an ambient condition [IPA, acetone, toluene, chloroform, dimethylformamide (DMF), methanol, and para-xylene] with different dose conditions (see the Supplementary Materials and table S1). According to the type and dosage of gas, we confirm the 5CB film (20 μm thick) to exhibit different rates of RCP-to-LCP conversion. Under a low-dose condition (one gas source), for instance, we measure the conversion to occur at around 1.3 s (chloroform), 1.6 s (acetone), 5.2 s (toluene), 13.9 s (IPA), 22.7 s (para-xylene), 58.3 s (methanol), and 136 s (DMF) (table S1). For higher dosage, faster response rates are observed.

Design of spin-encoded metaholograms with asymmetric spin-orbit interaction

The spin-encoded metasurface is designed on the basis of conventional Pancharatnam-Berry (PB)–phase modulation technique to exploit the inherent symmetry of spin and degrees of orbital interactions (*43*, *44*). This demands two different unit cells for the metasurface to be created in separate spaces, resulting in a total efficiency loss. The optical energy utilization becomes inefficient because only 50% of the unit cell structures of the metadevice are useful for a specific helicity of incident illumination. As a result, the maximal theoretical total efficiency of a conventional PB-phase–based metasurface device is only 50%. To overcome the optical energy loss, we designed the metasurface with spin encoding via the asymmetric coupling between the orbit degrees of photons and their spin rather than symmetric coupling. This allows all unit cell structures of the metadevice to operate for both LCP and RCP light, which, in turn, helps to break the conventional efficiency limit. The asymmetric coupling can be stimulated by defying the innate behavior of PB-phase metaatoms, i.e., breaking the symmetry of the geometric phase reversal using a specifically designed array of metaatoms for both LCP and RCP illumination. Therefore, an extra phase delay that is independent of the geometrical parameters is required (i.e., the rotation angle of the metaatom). Here, we use a retardation phase delay (also known as propagation phase) for certain metaatoms to achieve that. Thus, the total accumulated phase delay of the scattered electromagnetic light can be written as the linear combination of the retardation phase delay $\rho(x, y)$ and the PB-phase delay $2\sigma\zeta(x, y)$, i.e., $\rho(x, y) + 2\sigma\zeta(x, y)$, where $\zeta(x, y)$ is the orientation angle of the deployed metaatom and the helicity of the light defines the value of σ to be −1 and +1 for LCP and RCP, respectively. Note that the first term of the total phase delay is helicity independent. The careful optimization of individual metaatoms not only ensures the full independent control of the phase delay but also promises the generation of noncentral symmetric and distinct wavefronts, which maximize the optical energy usage of the metasurface designs. The concept of asymmetric coupling is achieved by optimizing a set of eight unit cells consisting of distinct nanoantennas made of a-Si:H on top of a glass substrate. The variables that change under the parametric sweep to gain the desired degrees of freedom are the length (L), width (w), orientation angle [$\zeta(x, y)$], and displacement (d) of the unit cell with a fixed height (h) of 400 nm. A perspective view of the sections of the proposed optimized metasurface is depicted in Fig. 2A. The confinement of magneto-electric resonances within the nanoantennas validates the optimization procedure (*45*). The criterion to select the size of the nanoantennas depends on the ability to retain a high transmission efficiency and a fixed incremental phase shift. A numerically obtained pseudo–colored two-dimensional (2D) plot for the working wavelength (of 633 nm) is illustrated in Fig. 2B and shows the efficiency (T_{LR}) of the transmitted LCP component under RCP incidence as a function of L and w of the nanoantenna. The geometric parameters of the selected nanoantennas for this work are highlighted as white dots in Fig. 2B. A set (consisting of two arrays of four preselected nanoantennas) is used such that the phase difference among neighboring unit cells remains fixed with a constant value of 45° as displayed in Fig. 2C.

Four of the eight designed unit cells in the set provide the required retardation phase delays, while the remaining four have the same dimensions but with an orientation angle of 90°. This arrangement produces a phase delay of 180° for every fourth nanoantenna

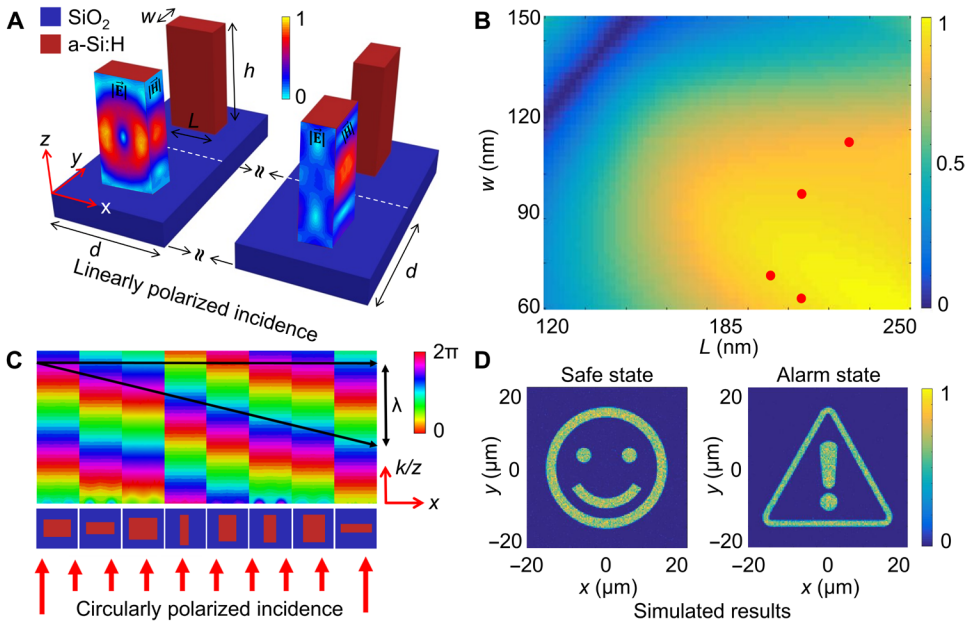

Fig. 2. Numerical optimization of asymmetric coupled metasurfaces. (**A**) Elements of the proposed metasurface consisting of a-Si:H nanoantennas showing the electric and magnetic field intensity distributions for the nanoantennas with their long axis parallel to the *x* axis (left element) and *y* axis (right element), under linearly polarized incidence. Height *h* and displacement *d* are fixed at 400 and 300 nm, respectively. (**B**) Efficiency (T_{LR}) of the transmitted LCP component under RCP incidence as a function of length (*L*) and width (*w*) of the nanoantennas. Red dots indicate the geometries of four selected unit cells that have high diffraction efficiency while taking fabrication resolution into account. (**C**) Full-phase coverage and wavefront modulation using the selected set of eight unit cells. (**D**) Calculated holograms for safe (smiley face, left) and alarm states (exclamation mark, right) obtained from the designed asymmetric coupled metasurface.

within the set. Note that the values of T_{LR} and $\rho(x, y)$ are independent of the variation in the orientation angles, which is the primary factor in achieving an asymmetric coupled metasurface. This arrangement of nanoantennas can be used to arbitrarily and independently manipulate the wavefront of light for both circularly polarized helicities. Suppose $Q_{-\sigma}(x, y)$ and $Q_{+\sigma}(x, y)$ denote the phase distributions of two distinct target images that are required to produce two unique holographic patterns under LCP and RCP, respectively, and are expressed as

$$Q_{\pm\sigma}(x,y) = \rho(x,y) \pm 2\zeta(x,y) \quad (1)$$

Equation 1 is the combination of two equations, which can be used to determine the values of $\rho(x, y)$ and $\zeta(x, y)$ through a simple substitution method

$$\rho(x,y) = \frac{Q_{+\sigma}(x,y) + Q_{-\sigma}(x,y)}{2} \quad (2)$$

$$\zeta(x,y) = \mathrm{mod}\left[\frac{Q_{-\sigma}(x,y) - Q_{+\sigma}(x,y)}{4}, 2\pi\right] \quad (3)$$

Every optimized unit cell along with its anisotropic nanoantenna is encrypted with the required retardation phase $\rho(x, y)$ and orientation angle $\zeta(x, y)$ corresponding to its location on the metasurface. We use 2D images to represent a "safety state" (smiley face) and "alarm state" (exclamation mark) to determine the phase distributions $Q_{+\sigma}(x, y)$ and $Q_{-\sigma}(x, y)$, respectively, using the Gerchberg-Saxton inverse Fourier transform algorithm. To validate the operation of the asymmetric coupled metasurface, a metahologram of 40.02 μm × 40.02 μm is numerically simulated using a commercially available full-wave electromagnetic simulation software (Lumerical Inc.). The reproduced optical images from the simulated asymmetric coupled metasurface for the safety state for RCP illumination and alarm state for LCP illumination are illustrated in Fig. 2D (left and right, respectively).

Demonstration of holographic gas sensors and wearable applications

The real-time visualization of gas exposure is demonstrated by the gas responsive LC-MS system (Fig. 3). The sensing capability, fast switching of the holographic image, and high diffraction efficiency of the LC-MS gas sensor are tested in the optical setup upon the exposure of volatile gas, where RCP light is illuminated on the sensor, as shown in Fig. 3A. To this end, we use a ubiquitous volatile gas source in our daily life, a board marker containing various organic solvents including IPA (Fig. 3B). The metahologram device consists of a-Si:H nanoantennas and has a footprint of 300 μm × 300 μm, as shown in Fig. 3C. In the absence of the volatile gas, the LC-MS sensor projects a smiling holographic image as a "safety sign." After the gas exposure, however, we observe an almost instantaneous switching of the safety sign to an exclamation mark as an "alarm sign." This happens because the volatile gases from the pen diffuse into the LC layer, which reduces the optical retardance, thus converting the polarization of the output beam from RCP to LCP, which requires the change in the retardation of half wavelength (= π radian). In addition, when the gas is removed, the hologram rapidly restores itself back to the safety sign as the LCs return to their initial orientation, as described in Fig. 3D (movie S3). The LC-MS gas sensor is confirmed to be able to switch the holographic image within a few seconds. As indicated above, the holographic images are switched at ~18 s under $C_{IPA} \approx 200$ ppm (Fig. 1, C to F) and at ~7 s under $C_{IPA} \approx 400$ ppm (movie S2). Because C_{IPA} introduced by the board

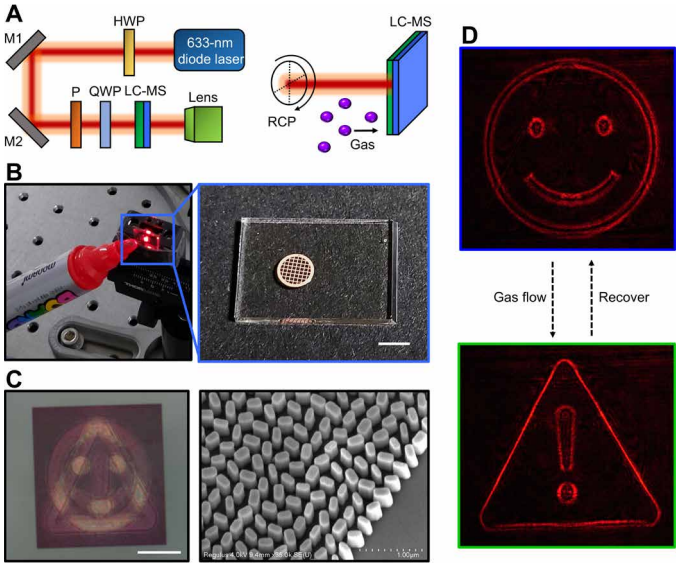

Fig. 3. Demonstration of an LC-MS gas sensor. (**A**) Optical setup for an LC-MS gas sensor (HWP, half wave plate; M1, mirror 1; M2, mirror 2; P, polarizer; QWP, quarter wave plate). In the absence of IPA gas, the RCP light illuminated on the LC-MS sensor passes the LC layer without any polarization conversion and is transmitted into the metasurface. In contrast, the LC layer converts the incoming RCP into LCP light upon the exposure of IPA gas. (**B**) Photographs of an LC-MS gas sensor with a board marker as a source of volatile gases including IPA. Scale bar, 3 mm. Photo credit: Inki Kim, POSTECH. (**C**) Optical and SEM images of the integrated dielectric metasurface. Scale bar, 100 μm. (**D**) Resulting holographic image alarms. Upon the exposure of gases from the board marker, the LC-MS sensor rapidly exhibits the alarm sign within a few seconds and recovers the initial safety sign once the gases are removed. See movie S3.

marker is likely lower than PEL of IPA (C_{IPA} = 400 ppm), we expect that the fast response is responsible for other additional types of volatile gases from the board marker. Furthermore, we perform iterative experiments to investigate the response time with the marker at different distances from the sensor and confirmed that it is largely unaffected, as seen in movie S3.

A diffraction efficiency of about 59% was measured, allowing the holographic image to be observed very clearly with the naked eye. The hologram efficiency measurement schematic is shown in fig. S1. The hologram efficiency η is calculated as $\eta = P_t/P_i$, where P_t is the transmitted power of holographic images measured in the power meter and P_i is the input beam power. We note that one can also design the LC cells to be stable in the transient state transmitting LCP by forming polymer networks within the LCs, which is a technique that is currently adopted in LC-based electronic papers (*46*, *47*). In this case, the LC-MS gas sensors would display the holographic alarm sign even after the gas has been removed. This kind of sensor would be useful for applications where the exposure to a harmful gas needs to be tracked, such as in the transportation or storage of gas-sensitive products.

We note here that light-emitting layers [e.g., organic light-emitting diode (LED) and quantum dot LED] and optical films (e.g., polarizer and color filter) are widely used in existing consumer electronics such as displays and cameras because they are considerably thin (few hundred nanometers to few hundred micrometers) and can be integrated onto substrates including curved surfaces. They can, therefore, enable the LC metaholograms to be not only fully functional under ambient or incoherent illumination but also miniaturized.

Furthermore, to extend the applicability of the proposed sensors toward wearable devices, a flexible metasurface is demonstrated using a one-step nanocasting process (Fig. 4A) (*48*, *49*). Unlike the conventional nanoimprinting method, a functionalized ultraviolet (UV)–curable resin containing titanium dioxide nanoparticles (TiO_2 NPs) with high–refractive index n is used. Noticeably, as the NP-resin composite (NPC) material exhibits a moderate refractive index ($n \approx 2.0$) with zero extinction coefficient over the entire visible spectrum, it can be used as a dielectric metasurface itself. Thus, without any complex and tedious nanofabrication processes, such as dielectric layer deposition, electron beam lithography, and the following etching process, it is possible to use the one-step nanocasting process to prepare the metasurface on any arbitrary substrates as seen in Fig. 4 (A to D), and it is also suitable for a mass-production manufacturing method.

As illustrated in Fig. 4A, to fabricate the NPC metasurface, a master stamp is coated with a self-assembled monolayer (SAM) to reduce the adhesion force so that a polymer mold can be separated easily (*50*). Hard polydimethylsiloxane (h-PDMS) is spin-coated onto the master stamp and thermally cured to replicate its metasurface structures. Because a single h-PDMS layer is too strong to be separated from the master stamp without fracture, additional PDMS is also coated on the h-PDMS layer. After separating the polymer mold from the master stamp, the TiO_2 NPC is spin-coated onto the polymer mold to uniformly fill the holes, and residual solvent of the NPC is removed. The polymer mold is then placed NPC side down on the flexible polyethylene terephthalate (PET) substrate. The mechanical stability and high UV transparency of the polymer mold allow the TiO_2 NPC to be casted using UV exposure with an appropriate pressure. During the curing process, the UV exposure polymerizes the monomers in the TiO_2 NPC. The residual solvent of NPC diffuses into the polymer mold because of its high permeability. The NPC adheres more strongly to the PET substrate than the polymer mold with low surface energy, so it can be detached easily. After the release of the polymer mold, the TiO_2 metasurface is left on the substrate. Detailed scanning electron microscopy (SEM) images of the fabricated TiO_2 NPC metasurface are shown in fig. S2.

As a proof of concept, a flexible and conformal holographic gas sensor is printed on a flexible PET film and attached to the curved surface of safety goggles as demonstrated in Fig. 4 (E to G). The geometric parameters of the NPC metasurface with a 1 μm height are optimized for 532 nm wavelength incident light in a similar way to the a-Si:H metasurface design (see the Supplementary Materials; figs. S3 to S5 and table S2). Although the NPC and a-Si:H metasurfaces are optimized for 532 and 633 nm, respectively, they can operate over a broad range of wavelengths (Fig. 5). The calculated and measured diffraction efficiency of the NPC at 532 nm are higher than that of a-Si:H (because the extinction coefficient of a-Si:H is 0.12, while that of NPC is around almost zero) (fig. S6). Given that some defects exist on the device, which are inevitably produced during the nanocasting process, the diffraction efficiency is degraded a little. Regardless, a clear holographic alarm can be observed as shown in Fig. 4 (H and I). As a future application, the proposed flexible and conformal gas sensor could be further miniaturized and integrated with a commercial head-mounted display equipped with a light source, waveguide, and corresponding diffractive optical elements to fully establish wearable and compact gas sensors. Particularly, because the holographic gas sensors operate without any additional complex mechanical and electronic devices, it will enable

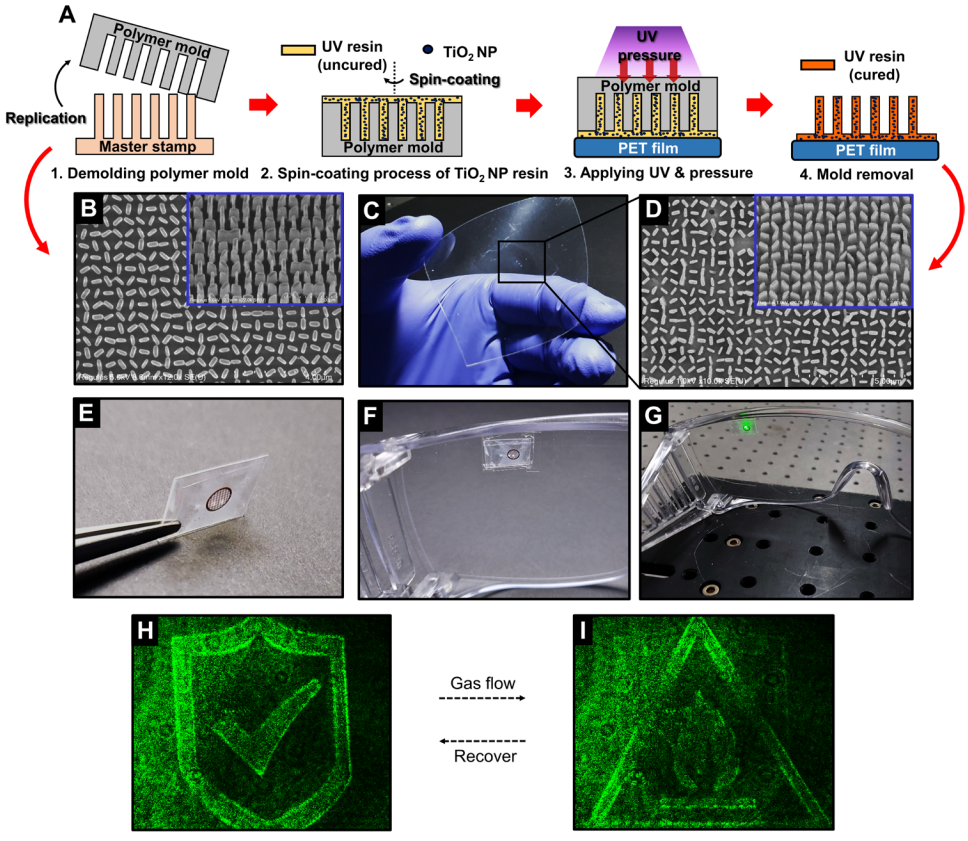

Fig. 4. Demonstration of a flexible LC-MS gas sensor and an integrated safety device. (**A**) Schematic illustration of a one-step nanocasting fabrication process of a flexible metasurface. The master stamp fabricated with 1 μm-height a-Si:H metasurface is chemically treated to reduce the adhesive strength for easier demolding process. The detached polymer mold is reusable. (**B**) SEM image (top view) of the silicon master stamp for the nanocasting process. The inset shows a tilted view image. (**C**) Photograph of the resulting flexible metasurface. (**D**) Corresponding SEM image (top view) of the NP-resin composite (NPC) metasurface. The inset shows a tilted view image. Photo credit: Inki Kim, POSTECH. (**E** to **G**) Flexible and conformal holographic metasurface gas sensor. The complete sensor, consisting of a flexible LC cell and an NPC metasurface, is attached onto the curved surface of safety goggles. Similar to the characterization of the a-Si:H metaholograms (Fig. 3), 532 nm wavelength RCP light is illuminated onto the flexible gas sensor to display holographic images. As seen in Fig. 5 (E and F), the LC cell and NPC metasurface are combined well. Photo credit: Inki Kim, POSTECH. (**H** and **I**) Experimentally demonstrated holographic safety signal in a normal condition and alarm signal upon an exposure of IPA gas. Compared to the a-Si:H device, the NPC metasurface not only has smaller critical dimensions and a larger height, meaning a higher aspect ratio, but also has some defects during the imprinting process. Thus, the diffraction efficiency and clearness of the holographic images are degraded.

low-cost (mass-producible with complementary metal-oxide semiconductor fabrication techniques) wearable gas sensors for factories, construction, and cleaning workers. Furthermore, the device can be operated in reflective mode, which may use ambient light instead of internal light source (e.g., laser or LED), making it more promising for cheaper, simpler, and miniaturized sensor platforms.

In this work, the aim is to offer a basis for gas-responsive metaholograms with proof-of-concept experiments, so we do not demonstrate the selectivity of the volatile gas. However, we note that the selective response for specific gases can be realized by functionalizing the LC interfaces. For example, LC films on metal salt-decorated substrates or metal substrates have been shown to change their internal molecular ordering (and thus the polarization of transmitted light) upon exposure of specific toxic gases such as dimethyl methylphosphonate, chlorine, and nitrogen dioxide (*8*, *51*–*54*). Also, functional amphiphiles or polymers that are decorated onto LC interfaces have been shown to provide general and versatile design principles for the LC systems with selective responsiveness. Specifically, the LC ordering can be altered via stimuli-induced conformational transition, cleavage, or intermolecular interactions of the functional molecules (*55*, *56*). In addition, previous works demonstrated the induced retardation change to be dependent on how much gas molecules diffuse into the LCs and disrupt the molecular ordering of LCs. Therefore, one can engineer the gas sensitivity of LC cells by tuning the molecular properties of LCs (e.g., diffusion coefficient, intermolecular interaction, and elasticity) that can be precisely and readily controlled via external stimuli, such as temperature, pressure, electric/magnetic fields, dopants, and chemical biding (*6*–*11*, *33*–*36*, *51*–*57*). A wide pool of LC phases having different internal ordering (and thus different physical/chemical characteristics) can be used.

We believe that these holographic gas sensors have advantages over conventional metasurface sensors in terms of their simple architectures, relieving the burden of data processing, and clear visual readouts that are promising for portable devices. Moreover, compared to previous LC sensors that signal the arrival of stimuli only via color or transmittance changes, our holographic gas sensor is capable of providing more intuitive and informative information as the metasurfaces can be designed to display images or visual cues that are relevant to their target application (*57*). For instance, rather

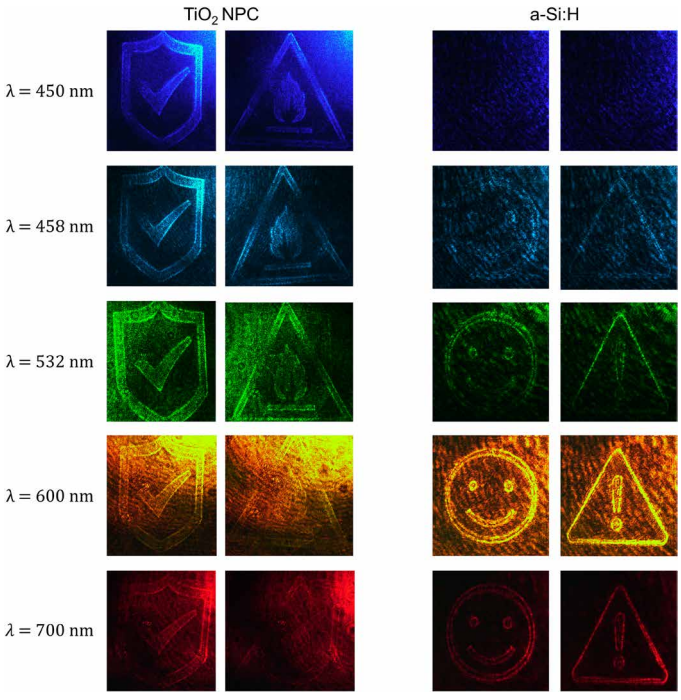

Fig. 5. Broadband responses of TiO_2 NPC and a-Si:H metasurfaces. The holographic images are produced by illuminating samples with a supercontinuum laser source. As shown, the NPC metasurface exhibits a higher contrast image below 532 nm and the a-Si:H metasurface produces a higher contrast image above 600 nm. The image contrast or diffraction efficiency is related to the material refractive index and the optimized metasurface geometric parameters.

than simply changing the color of the sensor, displaying holographic warning messages (e.g., "Don't touch", "Emergency," or "Wear a mask") or well-known warning symbols is much more effective for relaying emergency information to the user.

In summary, we propose general and versatile design rules to realize the potential of dynamically tunable and stimuli-responsive metasurface systems. In particular, we propose an LC-MS gas sensor platform for a rapid visual alarm system for toxic gas. By exploiting the prompt responsiveness of LCs for volatile gases and the ultracompact form factor of holographic metasurfaces, our designed gas sensors are verified in terms of their practicability and feasibility toward an ultracompact, cost-effective, and user-friendly gas sensor system that works without the requirements of any additional complex mechanical or electrical components. To provide high-quality holographic visual information, asymmetric coupled metasurface is designed, which produces a high diffraction efficiency (~59%) with very little cross-talk and/or afterimages between the "alarm" and "safety" signs. Furthermore, a flexible and conformal-type sensor realized by a one-step nanocasting process proves the feasibility of wearable sensor applications that can be applied to any kind of surface. We note that the LCs can be further functionalized by synthesizing a reactant-containing surfactant and treating it on the LC surface to make it selective for certain toxic gases. In addition, the use of orbital angular momentum–multiplexed metaholograms may increase the number of displaying channels, where multiple holographic warning signs can be displayed depending on the type and dosage of gas (*58*). Also, further developments of materials processing such as optimized a-Si:H growth (*59*) and silicon NPC (*60*) will improve the efficiency and extend the operation wavelength of the metaholograms. Finally, we expect that the wearable and ultracompact holographic gas sensor could be a vital platform to prevent gas poisoning accidents in various working and military environments by simply mounting the sensor onto the gloves or glasses of the user, giving them a prompt visual warning through the holographic alarms.

MATERIALS AND METHODS

Preparation of metasurfaces and master stamps

A 400 nm-thick layer of a-Si:H was deposited using plasma-enhanced chemical vapor deposition (BMR Technology HiDep-SC) with a flow rate of 10 standard cubic centimeter per minute (sccm) for SiH_4 and 75 sccm for H_2. For the master stamp fabrication, a 1 μm-thick a-Si:H layer was used. The nanobar-shaped metasurface design was transferred onto the positive tone photoresist (495 PMMA A2, MicroChem) using the standard electron beam lithography process (ELIONIX, ELS-7800; acceleration voltage: 80 kV, beam current: 100 pA). The exposed photoresist patterns were developed in methyl isobutyl ketone (MIBK)/IPA 1:3 developer solution for 12 min at 0°C. Then, a 50 nm-thick chromium (Cr) layer was deposited using electron beam evaporation (KVT, KVE-ENS4004). The lifted-off Cr nanobars were used as an etching mask for the a-Si:H layer, and the Cr patterns were transferred onto the a-Si:H layer using a dry etching process (DMS, silicon/metal hybrid etcher). The remaining Cr etch mask was removed by Cr etchant (CR-7).

Synthesis of TiO_2 NPC

The TiO_2 NP-resin composite was produced by mixing a TiO_2 NP-dispersed solution (DT-TIOA-30MIBK, Ditto Technology), monomer (dipentaerythritol penta-/hexa-acrylate, Sigma-Aldrich), and photo-initiator (1-hydroxycyclohexyl phenyl ketone, Sigma-Aldrich). The mixing ratio was adjusted to achieve a weight ratio of 4 weight % (wt %) for TiO_2 NPs, 0.7 wt % for the monomer, and 0.3 wt % for the photo-initiator.

One-step nanocasting process for NPC metasurfaces

To improve the mold release during the replication step, the master stamp, made of a 1 μm-thick a-Si:H metasurface, was coated using liquid-phase SAM in a solution mixture of a 1000:1 volume ratio of hexane and (heptadecafluoro-1,1,2,2-tetra-hydodecyl)trichlorosilane (H5060.1, JSI Silicone) for 10 min. To enhance a replication resolution, the h-PDMS solution was prepared by mixing 3.4 g of vinylmethyl copolymers (VDT-731, Gelest), 18 μl of platinum catalyst (SIP6831.2, Gelest), 0.1 g of modulator (2,4,6,8-tetramethyl2,4,6,8-tetravinylcyclotetrasiloxane, Sigma-Aldrich), 2 g of toluene, and 1 g of siloxane-based silane reducing agent (HMS-301, Gelest). The h-PDMS solution was spin-coated on the master stamp with 3000 rpm for 50 s and then cured at 70°C for 2 hours. To separate an h-PDMS layer from the master stamp without fracture, an additional PDMS layer was coated on the h-PDMS layer. The PDMS layer was prepared by coating a degassed mixture of a 10:1 weight ratio of PDMS (Sylgard 184 A, Dow Corning) and curing agent (Sylgard 184 B, Dow Corning) followed by a curing process at 110°C for 1 hour. The replicated h-PDMS polymer mold was released from the master stamp and then coated with vapor-phase SAM of (tridecafluoro-1,1,2,2-tetrahydrooctyl)trichlorosilane (SIT8174.0, Gelest) for 30 min at 5 torr followed by deionized water vaporization for 10 min at 10 torr. TiO_2 NPC (0.4 ml) was spin-coated on the

polymer mold with 2000 rpm for 30 s to uniformly fill the holes. The residual solvent of the NPC was removed. Last, the polymer mold was placed on a flexible PET substrate and pressed (where the TiO_2 NPC side faces toward the PET substrate) for 5 min at 2 bar with UV illumination (Nanosis 820, NND). The TiO_2 NPC metasurfaces were successfully transferred onto the PET substrate after demolding the polymer mold. Referring to the procedures previously described in (*49*), we further optimized the fabrication process of the TiO_2 NPC metasurfaces that were particularly designed for high-efficiency spin-encoded metaholograms.

Preparation of gas-responsive LC cells

For microfilms of 5CB (Figs. 1 and 3 to 5), the glass substrate was spin-coated by a polyimide (Nissan Chemical Korea) at 1000 rpm for 10 s followed by 2500 rpm for 30 s. The substrates were baked at 230°C for 50 min and then rubbed to achieve unidirectional tangential alignment of LCs. A 20 μm-thick copper grid for transmission electron microscopy (Electron Microscopy Sciences) was placed onto the substrate to prepare microwells and filled with a nematic LC, 5CB (Jiangsu Hecheng Display Technology Co. Ltd.). For side view experiments (insets of Fig. 1, C to E), the rubbed polyimide substrates were assembled in an antiparallel fashion. The gaps (200 to 300 μm) between the substrates were set by double-sided tape. The cells were filled with 5CB above the clearing temperature to avoid potential memory effects.

Calculation on the thickness of isotropic layer in 5CB film

In Fig. 1E, the thickness of isotropic layer was conversely calculated from the retardation value measured from the 5CB film upon the exposure of IPA gas. We assume the tilting angle of director to change linearly across the 5CB film. The pretilt angles of 5CB on the used planar polyimide and the air-LC interface were known to be 3.8° and 90°, respectively.

SUPPLEMENTARY MATERIALS

Supplementary material for this article is available at http://advances.sciencemag.org/cgi/content/full/7/15/eabe9943/DC1

REFERENCES AND NOTES

1. D. Sarkar, W. Liu, X. Xie, A. C. Anselmo, S. Mitragotri, K. Banerjee, MoS_2 field-effect transistor for next-generation label-free biosensors. *ACS Nano* **8**, 3992–4003 (2014).
2. C. Wu, A. B. Khanikaev, R. Adato, N. Arju, A. A. Yanik, H. Altug, G. Shvets, Fano-resonant asymmetric metamaterials for ultrasensitive spectroscopy and identification of molecular monolayers. *Nat. Mater.* **11**, 69–75 (2012).
3. P. W. Barone, S. Baik, D. A. Heller, M. S. Strano, Near-infrared optical sensors based on single-walled carbon nanotubes. *Nat. Mater.* **4**, 86–92 (2005).
4. J. M. Azzarelli, K. A. Mirica, J. B. Ravnsbaek, T. M. Swager, Wireless gas detection with a smartphone via rf communication. *Proc. Natl. Acad. Sci. U.S.A.* **111**, 18162–18166 (2014).
5. C. Esteves, E. Ramou, A. R. P. Porteira, A. J. M. Barbosa, A. C. A. Roque, Seeing the unseen: The role of liquid crystals in gas-sensing technologies. *Adv. Opt. Mater.* **8**, 1902117 (2020).
6. E. Bukusoglu, M. B. Pantoja, P. C. Mushenheim, X. Wang, N. L. Abbott, Design of responsive and active (soft) materials using liquid crystals. *Annu. Rev. Chem. Biomol. Eng.* **7**, 163–196 (2016).
7. J. T. Hunter, N. L. Abbott, Adsorbate-induced anchoring transitions of liquid crystals on surfaces presenting metal salts with mixed anions. *ACS Appl. Mater. Interfaces* **6**, 2362–2369 (2014).
8. T. Szilvási, N. Bao, K. Nayani, H. Yu, P. Rai, R. J. Twieg, M. Mavrikakis, N. L. Abbott, Redox-triggered orientational responses of liquid crystals to chlorine gas. *Angew. Chem. Int. Ed.* **57**, 9665–9669 (2018).
9. S. Sivakumar, K. L. Wark, J. K. Gupta, N. L. Abbott, F. Caruso, Liquid crystal emulsions as the basis of biological sensors for the optical detection of bacteria and viruses. *Adv. Funct. Mater.* **19**, 2260–2265 (2009).
10. C. Zafiu, Z. Hussain, S. Küpcü, A. Masutani, P. Kilickiran, E.-K. Sinner, Liquid crystals as optical amplifiers for bacterial detection. *Biosens. Bioelectron.* **80**, 161–170 (2016).
11. Y.-K. Kim, X. Wang, P. Mondkar, E. Bukusoglu, N. L. Abbott, Self-reporting and self-regulating liquid crystals. *Nature* **557**, 539–544 (2018).
12. I. Kim, G. Yoon, J. Jang, P. Genevet, K. T. Nam, J. Rho, Outfitting next generation displays with optical metasurfaces. *ACS Photonics* **5**, 3876–3895 (2018).
13. H. Jeong, Y. Yang, H. Cho, T. Badloe, I. Kim, R.-M. Ma, J. Rho, Emerging advanced metasurfaces: Alternatives to conventional bulk optical devices. *Microelectron. Eng.* **220**, 111146 (2020).
14. Y. Lee, S.-J. Kim, H. Park, B. Lee, Metamaterials and metasurfaces for sensor applications. *Sensors* **17**, 1726 (2017).
15. J. N. Anker, W. P. Hall, O. Lyandres, N. C. Shah, J. Zhao, R. P. Van Duyne, Biosensing with plasmonic nanosensors. *Nat. Mater.* **7**, 442–453 (2008).
16. N. Liu, M. Mesch, T. Weiss, M. Hentschel, H. Giessen, Infrared perfect absorber and its application as plasmonic sensor. *Nano Lett.* **10**, 2342–2348 (2010).
17. N. Liu, M. L. Tang, M. Hentschel, H. Giessen, A. P. Alivisatos, Nanoantenna-enhanced gas sensing in a single tailored nanofocus. *Nat. Mater.* **10**, 631–636 (2011).
18. S.-H. Oh, H. Altug, Performance metrics and enabling technologies for nanoplasmonic biosensors. *Nat. Commun.* **9**, 5263 (2018).
19. A. Kinkhabwala, Z. Yu, S. Fan, Y. Avlasevich, K. Müllen, W. E. Moerner, Large single-molecule fluorescence enhancements produced by a bowtie nanoantenna. *Nat. Photon.* **3**, 654–657 (2009).
20. H. Im, K. C. Bantz, S. H. Lee, T. W. Johnson, C. L. Haynes, S.-H. Oh, Self-assembled plasmonic nanoring cavity arrays for SERS and LSPR biosensing. *Adv. Mater.* **25**, 2678–2685 (2013).
21. S. Gwo, C.-Y. Wang, H.-Y. Chen, M.-H. Lin, L. Sun, X. Li, W.-L. Chen, Y.-M. Chang, H. Ahn, Plasmonic metasurfaces for nonlinear optics and quantitative SERS. *ACS Photonics* **3**, 1371–1384 (2016).
22. F. Neubrech, C. Huck, K. Weber, A. Pucci, H. Giessen, Surface-enhanced infrared spectroscopy using resonant nanoantennas. *Chem. Rev.* **117**, 5110–5145 (2017).
23. D. Rodrigo, A. Tittl, N. Ait-Bouziad, A. John-Herpin, O. Limaj, C. Kelly, D. Yoo, N. J. Wittenberg, S.-H. Oh, H. A. Lashuel, H. Altug, Resolving molecule-specific information in dynamic lipid membrane processes with multi-resonant infrared metasurfaces. *Nat. Commun.* **9**, 2160 (2018).
24. T. H. H. Le, T. Tanaka, Plasmonics–nanofluidics hydrid metamaterial: An ultrasensitive platform for infrared absorption spectroscopy and quantitative measurement of molecules. *ACS Nano* **11**, 9780–9788 (2017).
25. A. Tittl, A. Leitis, M. Liu, F. Yesikoy, D.-Y. Choi, D. N. Neshev, Y. S. Kivshar, H. Altug, Imaging-based molecular barcoding with pixelated dielectric metasurfaces. *Science* **360**, 1105–1109 (2018).
26. F. Yesilkoy, E. R. Arvelo, Y. Jahani, M. Liu, A. Tittl, V. Cevher, Y. Kivshar, H. Altug, Ultrasensitive hyperspectral imaging and biodetection enabled by dielectric metasurfaces. *Nat. Photon.* **13**, 390–396 (2019).
27. A. Leitis, A. Tittl, M. Liu, B. H. Lee, M. B. Gu, Y. S. Kivshar, H. Altug, Angle-multiplexed all-dielectric metasurfaces for broadband molecular fingerprint retrieval. *Sci. Adv.* **5**, eaaw2871 (2019).
28. J. Li, S. Kamin, G. Zheng, F. Neubrech, S. Zhang, N. Liu, Addressable metasurfaces for dynamic holography and optical information encryption. *Sci. Adv.* **4**, eaar6768 (2018).
29. P. Yu, J. Li, S. Zhang, Z. Jin, G. Schütz, C.-W. Qiu, M. Hirscher, N. Liu, Dynamic janus metasurfaces in the visible spectral region. *Nano Lett.* **18**, 4584–4589 (2018).
30. S.-J. Kim, I. Kim, S. Choi, H. Yoon, C. Kim, Y. Lee, C. Choi, J. Son, Y. W. Lee, J. Rho, B. Lee, Reconfigurable all-dielectric Fano metasurfaces for strong full-space intensity modulation of visible light. *Nanoscale Horiz.* **5**, 1088–1095 (2020).
31. C. Choi, S.-E. Mun, J. Sung, K. Choi, S.-Y. Lee, B. Lee, Hybrid state engineering of phase-change metasurface for all-optical cryptography. *Adv. Funct. Mater.* **31**, 2007210 (2020).
32. Y. Li, J. van de Groep, A. A. Talin, M. L. Brongersma, Dynamic tuning of gap plasmon resonances using a solid-state electrochromic device. *Nano Lett.* **19**, 7988–7995 (2019).
33. P. G. de Gennes, J. Prost, *The Physics of Liquid Crystals* (Clarendon Press, 1993).
34. M. Kleman, O. D. Lavrentovich, *Soft Matter Physics: An Introduction* (Springer, 2003).
35. B. Bahadur, *Liquid Crystals: Applications and Uses* (World Scientific, 1995).
36. D. Demus, J. Goodby, G. W. Gray, H.-W. Spiess, V. Vill, Chemical structure and mesogenic properties, in *Handbook of Liquid Crystals: Fundamentals* (Wiley-VCH, 1998).
37. Y. Lee, M.-K. Park, S. Kim, J. H. Shin, C. Moon, J. Y. Hwang, J.-C. Choi, H. Park, H.-R. Kim, J. E. Jang, Electrical broad tuning of plasmonic color filter employing an asymmetric-lattice nanohole array of metasurface controlled by polarization rotator. *ACS Photonics* **4**, 1954–1966 (2017).
38. D. R. Daniel, B. H. McAnalley, J. C. Garriott, Isopropyl alcohol metabolism after acute intoxication in humans. *J. Anal. Toxicol.* **5**, 110–112 (1981).
39. A. J. Lehman, H. F. Chase, The acute and chronic toxicity of isopropyl alcohol. *J. Lab. Clin. Med.* **29**, 561–567 (1944).
40. Y.-K. Kim, K. R. Raghupathi, J. S. Pendery, P. Khomein, U. Sridhar, J. J. de Pablo, S. Thayumanavan, N. L. Abbott, Oligomers as triggers for responsive liquid crystals. *Langmuir* **34**, 10092–10101 (2018).

41. S. Faetti, V. Palleschi, Nematic-isotropic interface of some members of the homologous series of 4-cyano-4'-(*n*-alkyl)biphenyl liquid crystals. *Phys. Rev. A* **30**, 3241–3251 (1984).
42. J. L. West, K. Zhang, A. Glushchenko, D. Andrienko, M. Tasinkevych, Y. Reznikov, Colloidal particles at a nematic-isotropic interface: Effects of confinement. *Eur. Phys. J. E* **20**, 237–242 (2006).
43. M. A. Ansari, I. Kim, D. Lee, M. H. Waseem, M. Zubair, N. Mahmood, T. Badloe, S. Yerci, T. Tauqeer, M. Q. Mehmood, J. Rho, A spin-encoded all-dielectric metahologram for visible light. *Laser Photon. Rev.* **13**, 1900065 (2019).
44. M. A. Ansari, I. Kim, I. D. Rukhlenko, M. Zubair, S. Yerci, T. Tauqeer, M. Q. Mehmood, J. Rho, Engineering spin and antiferromagnetic resonances to realize an efficient direction-multiplexed visible meta-hologram. *Nanoscale Horiz.* **5**, 57–64 (2020).
45. Z. Li, I. Kim, L. Zhang, M. Q. Mehmood, M. S. Anwar, M. Saleem, D. Lee, K. T. Nam, S. Zhang, B. Luk'yanchuk, Y. Wang, G. Zheng, J. Rho, C.-W. Qiu, Dielectric meta-holograms enabled with dual magnetic resonances in visible light. *ACS Nano* **11**, 9382–9389 (2017).
46. M. Moirangthem, A. F. Scheers, A. P. H. J. Schenning, A full color photonic polymer, rewritable with a liquid crystal ink. *Chem. Commun.* **54**, 4425–4428 (2018).
47. H. Xing, X. Wang, J. Xu, J. Wei, J. Guo, Polymer network microstructures and electro-optical properties of a pressure-sensitive cholesteric liquid crystal device. *RSC Adv.* **3**, 17822–17828 (2013).
48. K. Kim, G. Yoon, S. Baek, J. Rho, H. Lee, Facile nanocasting of dielectric metasurfaces with sub-100 nm resolution. *ACS Appl. Mater. Interfaces* **11**, 26109–26115 (2019).
49. G. Yoon, K. Kim, D. Huh, H. Lee, J. Rho, Single-step manufacturing of hierarchical dielectric metalens in the visible. *Nat. Commun.* **11**, 2268 (2020).
50. W. Zhou, J. Zhang, Y. Liu, X. Li, X. Niu, Z. Song, G. Min, Y. Wan, L. Shi, S. Feng, Characterization of anti-adhesive self-assembled monolayer for nanoimprint lithography. *Appl. Surf. Sci.* **255**, 2885–2889 (2008).
51. K. Nayani, Y. Yang, H. Yu, P. Jani, M. Mavrikakis, N. L. Abbott, Areas of opportunity related to design of chemical and biological sensors based on liquid crystals. *Liq. Cryst. Today* **29**, 24–35 (2020).
52. K. Nayani, P. Rai, N. Bao, H. Yu, M. Mavrikakis, R. J. Twieg, N. L. Abbott, Liquid crystals with interfacial ordering that enhances responsiveness to chemical targets. *Adv. Mater.* **30**, 1706707 (2018).
53. T. Szilvási, L. T. Roling, H. Yu, P. Rai, S. Choi, R. J. Twieg, M. Mavrikakis, N. L. Abbott, Design of chemoresponsive liquid crystals through integration of computational chemistry and experimental studies. *Chem. Mater.* **29**, 3563–3571 (2017).
54. A. Sen, K. A. Kupcho, B. A. Grinwald, H. J. VanTreeck, B. R. Acharya, Liquid crystal-based sensors for selective and quantitative detection of nitrogen dioxide. *Sens. Actuators B Chem.* **178**, 222–227 (2013).
55. Y.-T. Lai, J.-C. Ku, Y.-J. Yang, A novel gas sensor using polymer-dispersed liquid crystal doped with carbon nanotubes. *Sens. Actuators A Phys.* **215**, 83–88 (2014).
56. Y.-K. Kim, Y. Huang, M. Tsuei, X. Wang, N. C. Gianneschi, N. L. Abbott, Multi-scale responses of liquid crystals triggered by interfacial assemblies of cleavable homopolymers. *ChemPhysChem* **19**, 2037–2045 (2018).
57. I. Kim, M. A. Ansari, M. Q. Mehmood, W.-S. Kim, J. Jang, M. Zubair, Y.-K. Kim, J. Rho, Stimuli-responsive dynamic metaholographic displays with designer liquid crystal modulators. *Adv. Mater.* **32**, 2004664 (2020).
58. H. Ren, X. Fang, J. Jang, J. Bürger, J. Rho, S. A. Maier, Complex-amplitude metasurface-based orbital angular momentum holography in momentum space. *Nat. Nanotechnol.* **15**, 948–955 (2020).
59. Y. Yang, G. Yoon, S. Park, S. D. Namgung, T. Badloe, K. T. Nam, J. Rho, Revealing structural disorder in hydrogenated amorphous silicon for a low-loss photonic platform at visible frequencies. *Adv. Mater.* **33**, 2005893 (2021).
60. G. Yoon, X. Kim, S.-U. Kim, S. Han, H. Lee, J. Rho, Printable nanocomposite metalens for high-contrast near-infrared imaging. *ACS Nano* **15**, 698–706 (2021).

Acknowledgments

Funding: This work was financially supported by the National Research Foundation (NRF) grants (NRF-2019R1A2C3003129, CAMM-2019M3A6B3030637, NRF-2019R1A5A8080290, and NRF-2018M3D1A1058997) funded by the Ministry of Science and ICT (MSIT) of the Korean government. Y.-K.K. acknowledges the NRF grant (NRF-2020R1F1A1066377) funded by the MSIT of the Korean government. I.K. acknowledges the NRF Sejong Science fellowship (NRF-2021R1C1C2004291) funded by the MSIT of the Korean government. Y.K. acknowledges a fellowship from the Hyundai Motor Chung Mong-Koo Foundation. **Author contributions:** J.R., Y.-K.K., and I.K. conceived the idea and initiated the project. I.K., J.R., and Y.-K.K. developed the process and designed the experiment. I.K., M.A.A., M.Q.M., and T.B. designed the holograms and conducted numerical simulations. I.K., W.-S.K., and J.G. fabricated the devices. I.K., W.-S.K., and Y.K. performed the optical characterizations. K.K. and H.L. fabricated flexible metasurfaces. I.K., J.R., and Y.-K.K. analyzed data and mainly wrote the manuscript. J.R. guided the entire research. All authors participated in discussion and confirmed the final manuscript. **Competing interests:** The authors declare that they have no competing interests. **Data and materials availability:** All data needed to evaluate the conclusions in the paper are present in the paper and/or the Supplementary Materials. Additional data related to this paper may be requested from the authors.

Submitted 28 September 2020
Accepted 22 February 2021
Published 7 April 2021
10.1126/sciadv.abe9943

Citation: I. Kim, W.-S. Kim, K. Kim, M. A. Ansari, M. Q. Mehmood, T. Badloe, Y. Kim, J. Gwak, H. Lee, Y.-K. Kim, J. Rho, Holographic metasurface gas sensors for instantaneous visual alarms. *Sci. Adv.* **7**, eabe9943 (2021).